coatings

MDPI

Article

Formation of Solid Lubricants during High Temperature Tribology of Silver-Doped Molybdenum Nitride Coatings Deposited by dcMS and HIPIMS

Martin Fenker [1,*], Martin Balzer [1], Sabine Kellner [2], Tomas Polcar [3], Andreas Richter [1], Frank Schmidl [2] and Tomas Vitu [3]

[1] Research Institute for Precious Metals and Metal Chemistry, 73527 Schwäbisch Gmünd, Germany; balzer@fem-online.de (M.B.); richter@fem-online.de (A.R.)
[2] Low Temperature Physics Group, Institute of Solid State Physics, Friedrich Schiller University Jena, 07743 Jena, Germany; sabine.kellner@uni-jena.de (S.K.); frank.schmidl@uni-jena.de (F.S.)
[3] Department of Control Engineering, Faculty of Electrical Engineering, Czech Technical University in Prague, 16627 Prague, Czech Republic; polcatom@fel.cvut.cz (T.P.); tomas.vitu@fel.cvut.cz (T.V.)
* Correspondence: fenker@fem-online.de

Abstract: The coating system MoN-Ag is an interesting candidate for industrial applications as a low friction coating at elevated temperatures, due to the formation of lubricous molybdenum oxides and silver molybdates. Film deposition was performed by high-power impulse magnetron sputtering and direct current magnetron sputtering. To facilitate a future transfer to industry Mo-Ag composite targets have been sputtered in Ar/N_2 atmosphere. The chemical composition of the deposited MoN-Ag films has been investigated by wavelength dispersive X-ray spectroscopy. Morphology and crystallographic phases of the films were studied by scanning electron microscopy and X-ray diffraction. To obtain film hardness in relation to Ag content and bias voltage, the instrumented indentation test was applied. Pin-on-disc tribological tests have been performed at room temperature and at high temperature (HT, 450 °C). Samples from HT tests have been analyzed by Raman measurements to identify possible molybdenum oxide and/or silver molybdate phases. At low Ag contents (≤7 at.%), coatings with a hardness of 18–31 GPa could be deposited. Friction coefficients at HT decreased with increasing Ag content. After these tests, Raman measurements revealed the MoO_3 phase on all samples and the $Ag_2Mo_4O_{13}$ phase for the highest Ag contents (~23–26 at.%).

Keywords: PVD; HiPIMS; wear resistant coating; low friction coatings; tribology

Citation: Fenker, M.; Balzer, M.; Kellner, S.; Polcar, T.; Richter, A.; Schmidl, F.; Vitu, T. Formation of Solid Lubricants during High Temperature Tribology of Silver-Doped Molybdenum Nitride Coatings Deposited by dcMS and HIPIMS. *Coatings* **2021**, *11*, 1415. https://doi.org/10.3390/coatings11111415

Academic Editors: Joerg Vetter and Richard P. Welty

Received: 26 October 2021
Accepted: 17 November 2021
Published: 19 November 2021

1. Introduction

The current interest in Mo_xN coatings for tribological applications results from its excellent mechanical properties (hardness 21–39 GPa compared to 18–24 GPa for TiN and CrN [1–3]) and its friction-reducing and lubricating qualities of the surface oxides at elevated temperatures (>300 °C) which is due to the presence of lamellar structures (also Magnéli phases [4]) that shear easily during contact loading. Three molybdenum nitride phases are stable in thermal equilibrium according to H. Jehn et al. [5]—tetragonal β-Mo_2N, face-centered cubic γ-Mo_2N and hexagonal δ-MoN. Up to now, no single phase δ-MoN could be synthesized by reactive magnetron sputtering [6–9]. The high hardness and relatively low coefficient of friction (COF) of Mo_xN coatings of about 0.25–0.4 against alumina balls [2,10] leads to an excellent wear resistance at lower temperatures [2,3,10,11]. Adding silver to molybdenum nitride is interesting for high temperature (HT) tribological applications for three reasons:

1. The MoN-Ag coatings oxidize and form lamellar MoO_3 and play a key role in the friction reduction at HT friction processes [10];

2. Low melting point Ag molybdates can synthesize, which also strongly reduces friction [12]; and
3. Ag exhibits low shear strength and has already been used as a solid lubricant in high-temperature tribological applications [13,14].

Up to now, several papers have been published on the topic of MoN-Ag films deposited by magnetron sputtering from elemental target materials [3,15–18] or mosaic targets [19,20]. The optimal concentration of Ag significantly improves the mechanical and tribological properties of parts subjected to tribological load [3]. A slight hardness increase is observed for Ag additions of a few percent using reactive magnetron sputtering [15,19]. However, at higher Ag contents (>15 at.%) hardness of MoN-Ag films drops below 10 GPa [15]. Gulbiński et al. reported an optimal Ag content of about 6 at.% for the tribological behavior of MoN-Ag films at HT [15]. At this Ag content the hardness is still sufficiently high (20 GPa) and the friction coefficient is clearly lowered.

In this work, MoN and MoN-Ag films have been deposited by using direct current magnetron sputtering (dcMS) and high-power impulse magnetron sputtering (HiPIMS). The main aim of this work is to study the formation of solid lubricants in the coating system MoN-Ag by using two different deposition technologies, namely dcMS and HiPIMS. Pin-on-disk tests were performed at RT and HT to study the formation of lubricating films lowering the COF. To simplify the transfer from research to industry MoAg composite targets have been applied and their sputtering behavior has been explored. Neither HiPIMS nor composite targets have been reported previously for the deposition of MoN-Ag films.

2. Materials and Methods

2.1. Film Deposition

The MoN-Ag coatings were deposited onto mirror-polished high-speed steel samples (HSS M2, 1.3343, Werner Wilke Zerspanungstechnik GmbH, Homberg, Germany, hardness 64–66 HRC) by magnetron sputtering in a Leybold L560 UV system (Leybold AG, Alzenau, Germany, base pressure $<1.5 \times 10^{-3}$ Pa) using a Ø 75 mm sputtering cathode (PK75, Leybold Heraeus GmbH, Hanau, Germany, target area 44.2 cm^2). Two sputtering methods were applied: dcMS (power supply: ADL Maris GS30–1000, ADL GmbH, Darmstadt, Germany) and HiPIMS (power supply: MELEC SPIK 1000 A pulser, MELEC GmbH, Baden-Baden, Germany, powered by the same ADL Maris GS30–1000) using 2 different pulse patterns. The power supplies were operated at a fixed averaged power of 400 W (target power density: 9 W/cm^2). After plasma cleaning of the target and the substrates, a pure metallic adhesion layer—about 50 nm thick—was deposited from the target material that was used for the nitride layer (Mo or MoAg alloy target). The same parameters as for the nitride layer were used with the difference that only Ar gas with a slightly increased partial pressure (0.4 Pa) was used to stabilize the plasma. For the deposition of the nitride coatings, an Ar/N_2 gas mixture (gas purity 99.999%) was employed. The substrate holder was fixed at a distance of 6 cm opposite the target surface. No intentional heating was applied to the substrates. The substrate was kept at floating potential except for one series of depositions where the bias voltage was varied between −30 and −150 V. This DC bias voltage was provided by a second HiPIMS pulse unit (MELEC SIPP 2000A, MELEC GmbH, Baden-Baden, Germany) being capable of carrying a sufficiently high substrate current during the pulse on times.

Four series of samples were produced and process details are listed in Table 1:

1. Series dc-0.4: MoN and MoN-Ag films deposited by dcMS with a nitrogen partial pressure, $p(N_2)$, of 0.4 Pa and floating substrate bias voltage;
2. Series HiP-0.07: MoN and MoN-Ag films deposited by HiPIMS with $p(N_2)$ = 0.07 Pa and floating substrate bias voltage;
3. Series HiP-0.4: MoN and MoN-Ag films deposited by HiPIMS with $p(N_2)$ = 0.4 Pa and floating substrate bias voltage;
4. Series HiP-0.4-bias: Process "HiP-0.4", but with a variation of the substrate bias voltage from −30 to −150 V.

Table 1. Deposition parameters of the 4 series and the coating thickness d_{film} of the prepared films.

		Deposition Param.			HiPIMS Parameters			Thickness	
Series	**Target**	**Bias (V)**	**p(Ar) (Pa)**	**p(N_2) (Pa)**	**t_{on} (µs)**	**T (µs)**	**Duty Cycle**	**i_{peak} (A/cm²)**	**d_{film} (µm)**
dc-0.4	Mo	float.	0.3	0.4	-	-	100	0.022	1.9
	MoAg10							0.021	2.2
	MoAg20							0.019	1.7
	MoAg35							0.019	1.9
HiP-0.07	Mo	float.	0.3	0.07	30	2000	1.5	1.5	2.4
	MoAg10		0.37					1	2.1
	MoAg20							0.9	1.5
	MoAg35							0.9	1.9
HiP-0.4	Mo	float.	0.3	0.4	14	2000	0.7	3	2.1
	MoAg10				16		0.8	2	2.2
	MoAg20				20		1	1.5	1.7
	MoAg35				24		1.2	1.2	1.8
HiP-0.4-bias	MoAg35	float.	0.3	0.4	24	2000	1.2	1.2	1.8
	MoAg35	−30						1.1	2.1
	MoAg35	−100						1.1	2.0
	MoAg35	−150						1.1	2.0

The utilized target materials were elemental Mo targets and MoAg compound targets (Sindlhauser Materials GmbH, Kempten, Germany) with a purity of 99.95% and 99.8%, respectively. The MoAg compound targets have been manufactured by powder metallurgy and vacuum hot pressing. MoAg targets were ordered with 10, 20 and 35 at.% of silver (labeled as MoAg10, MoAg20 and MoAg35). The Ag content in the compound targets were measured by inductively coupled plasma optical emission spectroscopy (ICP-OES, Agilent 5110, Agilent Technologies Australia Pty Ltd, Melbourne, Australia) on chips which were milled from the target center. The measured Ag content for the MoAg10, MoAg20 and MoAg35 targets was about 7, 14 and 33 at.% as listed in Table 2.

Table 2. Silver content of the MoAg compound targets and of the deposited MoN-Ag coatings of the 3 series without substrate bias (measured by WDX, 7 keV).

Target	**Ag Content Target, C_{target} (Ag) (at.%)**	**Ag Content Coating, C_{coat} (Ag)**		
		dc-0.4 (at.%)	**HiP-0.07 (at.%)**	**HiP-0.4 (at.%)**
MoAg10	7	0.9	1.6	0.4
MoAg20	14	5.8	6.2	2.8
MoAg35	33	24.1	26.1	23.1

The pulse duration t_{on} had to be slightly increased with increasing Ag target content in Series HiP-0.4 in order to balance the increase of the target voltage, preventing it from approaching the maximum of the pulser (−1000 V) (for details, see Section 3.1).

2.2. Characterization

The film composition was measured by wavelength dispersive X-ray spectroscopy (WDX, INCA 5.05, Oxford Instruments, High Wycombe, UK) with a measuring field of 60 µm² with a field emission scanning electron microscope (FE-SEM, Zeiss Gemini SEM 300, Oberkochen, Germany). The electron accelerating voltage was adjusted to 7 kV for limiting the information depth, which was about 0.25 µm in this case. The Lα emission lines were analyzed for the elements Mo and Ag, and the Kα emission lines for N.

Crystallographic phases were studied by X-ray diffraction in Bragg-Brentano geometry (XRD, Bruker D8 DaVinci, Karlsruhe, Germany). More or less finely fragmented film debris received from (intentionally produced) badly adherent coatings (without metallic interlayer with the exception of sample dc-0.4/Mo target) were sprinkled on zero diffraction plates for

phase analysis. Due to the low amount of this film debris, milling could not be applied, and hence no real powder could be produced. However, the advantage of having the coatings as debris was to reduce the film texture, which distinctly enhances the identification of crystallographic phases.

The film hardness was measured by instrumented indentation test (Fischerscope H100 xy p, Sindelfingen, Germany with an upgraded EPROM for a reduced minimum load of 0.1 mN) using a Vickers indenter and 9 mN of maximum load. The durations for load increase, creeping under maximum load and decreasing load were 10 s, respectively. The penetration depth of the indenter varied between 0.12 µm for the hardest films (30 GPa) and 0.2 µm for the softest films (10 GPa). Adhesion was acquired by the Daimler Benz Rockwell C adhesion test (Dia Testor 2 Rc, Otto-Wolpert-Werke GmbH, Ludwigshafen, Germany, HF classification with 6 HF classes, for details see [21,22]).

Tribological measurements were carried out by pin-on-disc tribometers at room temperature (RT) or at a temperature of 450 °C (HT = high temperature) using two mechanically similar pin-on-disc machines (CSM Instruments SA, Peseux, Switzerland), one equipped with a heating stage (at CTU Prague) and one without (fem). All other test parameters were kept the same, i.e., counterpart: 6 mm Al_2O_3 ball, wear track diameter: 2 mm, load: 10 N, rotation speed: 500 min^{-1} (corresponds to a sliding speed of 52.4 mm/s). The measurement duration usually comprised 30,000 rotations with the exception of measurements on samples with MoN-Ag films with >20 at.% of Ag content, which were stopped after 5000 rotations due to worn coatings at RT. The sliding distance for the 5000 and 30,000 rotations amounts to 31.4 and 188.5 m, respectively. The coefficient of friction (COF) was recorded and averaged between 1000 and 30,000 or 1000 and 4500 rotations, respectively. In Figure 1 this is shown for two samples from the HiP-0.07 series at RT and HT for the case of 30,000 cycles. The wear was analyzed by confocal microscopy (Nanofocus µsurf custom, Oberhausen, Germany) using a 4 × 4 pattern of stitched scans. Wear volume and depth were evaluated by Mountains Map (Version 7.2.7568, 2015, Digital Surf, Besancon, France).

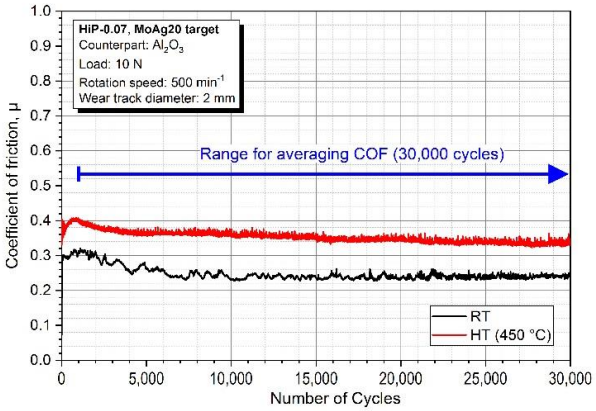

Figure 1. COF vs. number of cycles of MoN-Ag coated HSS samples. The samples used for this diagram are from the series HiP-0.07 (MoAg20 target). Pin-on-disk tests were performed at RT and at 450 °C.

Film thickness (see Table 1) was measured by tactile profilometry (MarSurf + MarSurf GD26+ BFW A 10-45-2/90°, Mahr GmbH, Göttingen, Germany) on a sharp film edge, produced by covering a part of the samples with a razor blade during deposition. This sample was always fixed at the same position at the substrate holder.

The thickness of the oxide films evolving during the HT tribological tests was determined by two methods:

1. Glow discharge optical emission spectroscopy (GDOES, GDA 750, SPECTRUMA Analytik GmbH, Hof, Germany) for thin oxide films on Ag-free Mo_xN films;
2. Optical profilometry (Nanofocus µsurf custom + Mountains Map, see above) on ball crater wear tracks for the other samples.

For the latter, a ball crater was ground into the samples (aside from the worn area) using a CSM Calotest (Peseux, Switzerland) with a 100Cr6 steel ball (Ø 40 mm) and 0.1 µm diamond paste. The oxide layers turned out to be well visible. At the transition between non-oxidized MoN-Ag film and the oxide layer, a more or less pronounced plateau emerged, where the oxide is removed quite uniformly. The entire ball crater was scanned by confocal microscopy (Nanofocus µsurf custom) and the height difference between this plateau and the surface of the surrounding sample surface was measured at up to eight measuring points.

Raman measurements were performed after high temperature tribological tests to identify molybdenum oxide and/or silver molybdate phases. Macro Raman measurements were carried out using a Renishaw inVia Raman spectrometer (Wotton-under-Edge, UK, laser wavelength: 532 nm, spot diameter 1.1–1.6 mm), gathering information from the sample surfaces outside the wear tracks. Furthermore, to collect phase information across the wear track, micro Raman measurements have been analyzed at several positions across the wear track on selected samples by using a Horiba XploRA Plus spectrometer (Lille, France, laser wavelength: 532 nm, spot sizes: 5 and 30 µm). Raman spectra were manually corrected for the baseline, as even repeated measurements at the same position could contain different underground signal heights.

3. Results and Discussion

3.1. Sputtering Behavior of Mo and MoAg Targets

In Figure 2 the HiPIMS pulse shapes of the cathode voltage and current of the Mo and the three different MoAg targets are depicted. As an example, the HiPIMS pulse with on-time t_{ON} = 30 µs and pulse duration T = 2000 µs was selected. Oscillations on all curves for the first 10 µs and a delay of the current increase of about 6 µs can be observed. However, after 10 µs the oscillations vanish and a stable plasma behavior establishes. In the stable pulse area, the cathode voltage increases with increasing Ag content in the targets from −700 V for the Mo targets towards –960 V for the MoAg35 target. The cathode current saturates for the MoAg targets after about half of t_{ON} but not for the Mo target. Obviously, the Ag in the composite targets significantly influences the sputtering behavior. Ag is known for having the highest sputtering yield of all metallic materials [23]. According to A. Anders [23], the discharge pulse will be dominated by gas ions for short pulses (as in our case) and self-sputtering will only occur for longer pulses. The peak power of the HiPIMS pulses decreases with increasing Ag content from about 43 kW for the Mo target towards about 30 kW for the MoAg35 target.

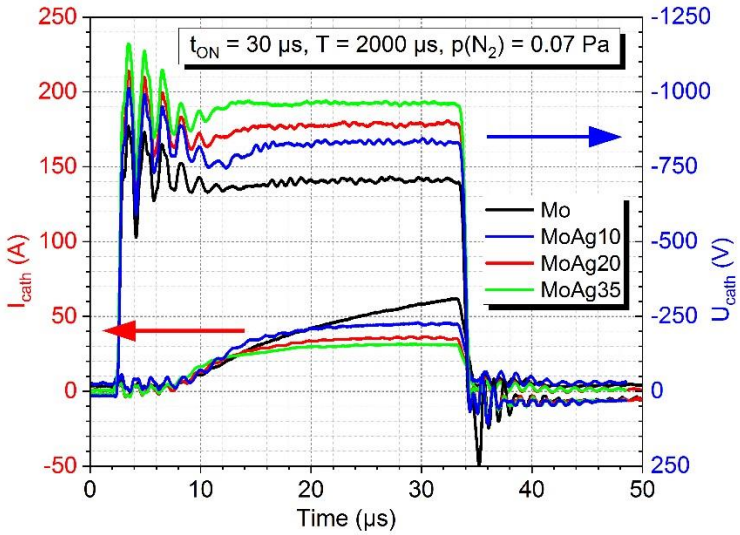

Figure 2. Cathode voltage and current for the HiPIMS pulse with 30 µs t_{ON} and a pulse duration of 2000 µs for Mo and the 3 different MoAg targets.

The comparison of the Ag/Mo ratio in the MoAg compound targets with the Ag/Mo ratio in the deposited MoN-Ag coatings revealed that a significant loss of Ag during sputtering (see Table 2 and Figure 3) is only observed for the MoAg10 and MoAg20 targets. For these targets, the most severe loss is found for the HIP-0.4 sputtering process. However, the Ag/Mo ratio in the film is higher compared to the target material for the MoAg35 target.

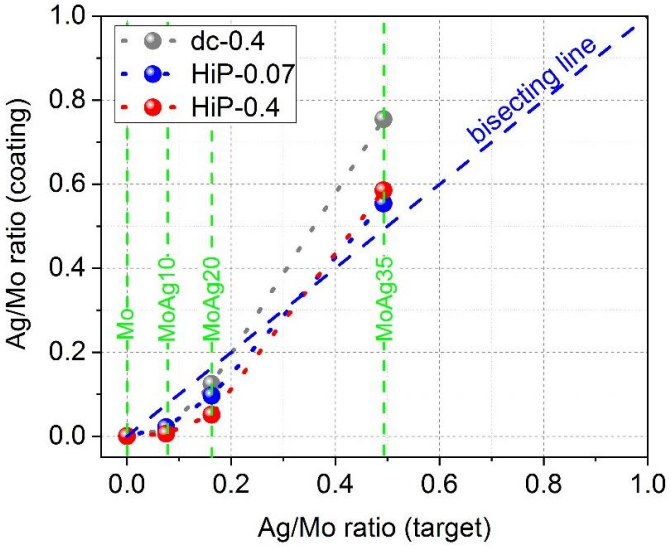

Figure 3. Ag/Mo ratio of coating vs. target. The dotted lines are a guide to the eye. A dashed bisecting line has been added. This dashed line represents the case when the Ag/Mo ratio in the coating resembles the one of the composite target. The green text and vertical dashed lines mark the corresponding target materials.

The high sputtering yield of Ag leads to an increase of the deposition rate of MoN-Ag coatings with increasing Ag content (Figure 4). As expected and in detail explained by A. Anders [24], the highest deposition rates are observed for the dc sputtered films (series dc-0.4). The higher deposition rates of series HiP-0.07 compared to series HiP-0.4 results from lower target poisoning (lower nitrogen partial pressure) and the slightly higher duty cycle (1.5% for HiP-0.07 compared to 0.7–1.2% for HiP-0.4). The latter relation was already reported by Haye et al. [25].

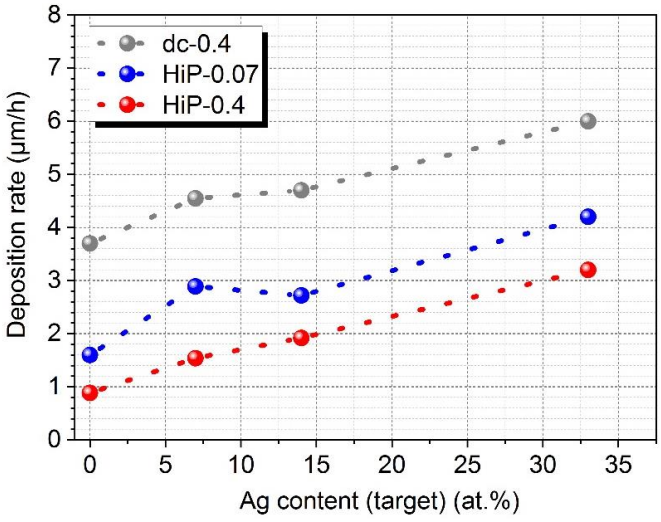

Figure 4. Deposition rate vs. Ag content (target) of MoN and MoN-Ag coatings.

3.2. Chemical Composition of MoN and MoN-Ag Coatings

The chemical composition of the MoN-Ag films deposited by the three different sputtering processes with floating substrate bias are presented in Figure 5. The silver content of the coatings was already listed in Table 2. It was observed that the incorporation of Ag into the films leads to a reduction of the N content in the films by up to 14 at.%. However, the N content in the MoN-Ag films is not drastically affected by changing the MoAg compound targets, i.e., by changing the Ag content in the MoN-Ag films. The highest Mo content is found for the films deposited with the MoAg10 target, which in case of HIPIMS is caused by the drastic decrease of the N content, when replacing the Mo by the MoAg10 target. By increasing C_{coat} (Ag) the Mo content decreases quite linearly with increasing C_{target} (Ag) (Figure 5). To understand and visualize the influence of C_{coat} (Ag) on the N/Mo ratio of the MoN-Ag films a graph has been compiled with the N/Mo ratio vs. C_{coat} (Ag) in Figure 6. Using the Mo_xN films as a starting point, it can be observed that incorporating a low content Ag into the films (MoAg10 compound target) leads to a significant decrease of the N/Mo ratio. A further increase of the Ag content leads to an increasing N/Mo ratio, reaching the original N/Mo ratio of the Mo_xN films with the exception of the dc-0.4 series. For the latter, a surplus of nitrogen is found in the MoN-Ag film deposited with the MoAg35 target, as the N/Mo ratio is higher than 1:1. For this MoN-Ag film, MoN is over-stoichiometric with respect to nitrogen.

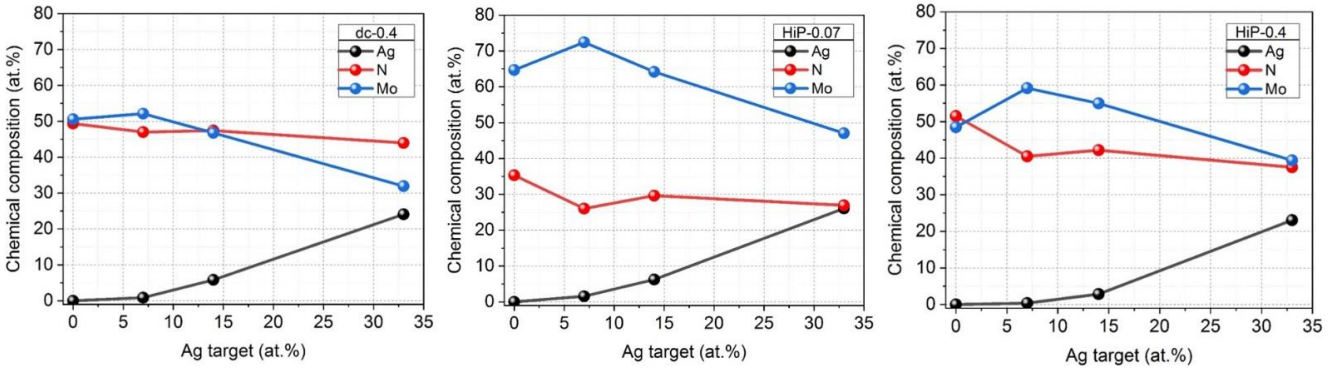

Figure 5. Chemical composition (WDX) of Mo and MoN-Ag coatings from the 3 different sputtering processes.

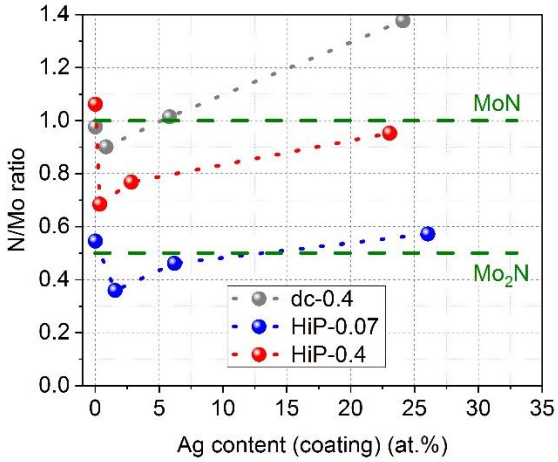

Figure 6. N/Mo ratio vs. Ag content of the coatings as measured by WDX. The horizontal dashed lines (olive color) indicate the N/Mo ratio of stoichiometric Mo_2N and MoN films.

3.3. Microstructure and Morphology

For all MoN and MoN-Ag samples, fracture cross section has been prepared and studied by SEM, see Figure 7 (samples with floating substrate bias) and Figure 8 (series HiP-0.4-bias). The Ag-free films without bias (Figure 7) show a fine-grained columnar

structure. Incorporating Ag into the films seems to densify the film microstructure. For MoN-Ag films deposited with MoAg20 and MoAg35 targets, the columnar structure vanishes. Ag precipitations in MoN-Ag films can only be observed for the one deposited by dcMS (series dc-0.4, target MoAg35). As reported in Section 3.1, for this sample, an over-stoichiometric MoN phase was identified in the MoN-Ag film.

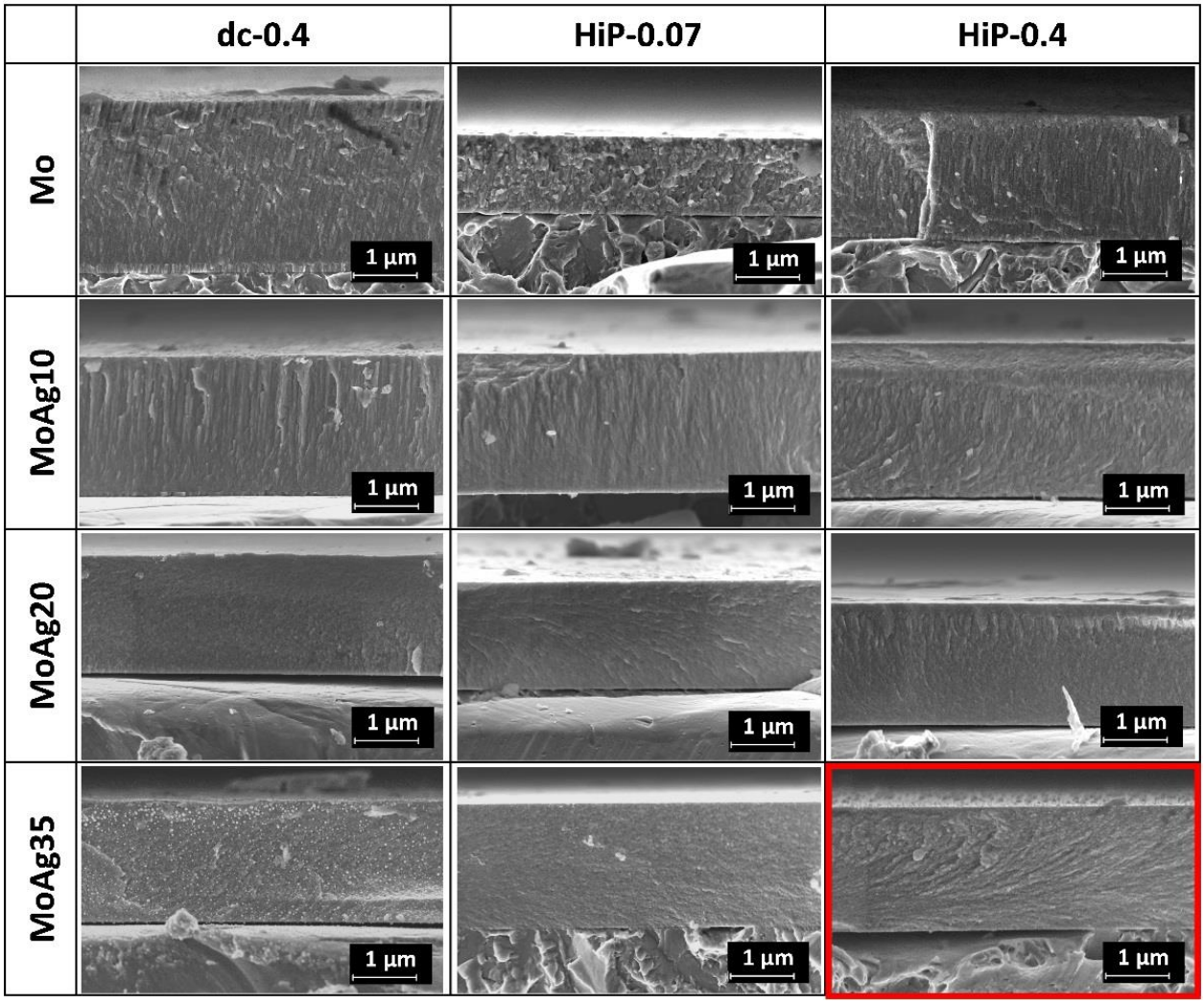

Figure 7. SEM micrographs of fracture cross sections of the samples from the 3 series with floating substrate bias voltage.

For studying the influence of substrate bias on the MoN-Ag microstructure a sample of the HiP-0.4 series with Ag content of 23.1 at.% (target MoAg35) was used as starting point. Figure 8 presents the development of the microstructure with increasing bias voltage (from left to right). The left SEM micrograph of the fractures' cross sections (=starting point) in Figure 8 shows a section of the SEM micrograph marked by a red box in Figure 7. Obviously, the increasing bias voltage densifies the films microstructure, even rendering the films featureless at bias voltages > −30 V. The increased ion bombardment causes this densification due to the applied substrate bias voltage [26,27]. The influence of the bias voltage on the Ag content in the MoN-Ag films will be discussed in the next subsection.

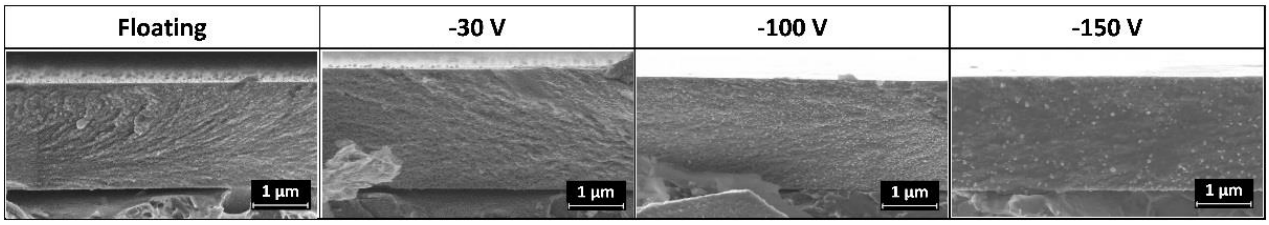

Figure 8. SEM micrographs of fracture cross sections of the samples from the bias voltage series (HiP-0.4-bias, MoAg35).

XRD investigations have been performed on the film debris and can be found in Figure 9. In Figure 9a the XRD patterns of films sputtered by dcMS are depicted (series dc-0.4). For the Ag-free MoN film two phases have been identified: Mo and δ-MoN. The Mo phase originates from the Mo adhesion layer. The peaks of the δ-MoN phase are slightly shifted to lower angles, indicating residual stress in the film debris. Incorporation of 0.9 at.% of Ag into the MoN film changes the Mo-N phase composition towards a mixture of γ-Mo_2N and δ-MoN, as observed for the MoN-Ag film sputtered from a MoAg10 target. The peaks of both phases are shifted to lower angles. A further increase of the Ag content to 5.8 at.% (target MoAg20) reduces the δ-MoN phase and increases the γ-Mo_2N phase, which can, for example, be witnessed for the (002) γ-Mo_2N peak and for the (210) δ-MoN peak. There are even signs of Ag precipitation at the 2θ angles 38°, 44.3° and 64.5° (asymmetric Mo_xN peaks). A significant change in the X-ray pattern is found when the MoAg35 target is used to deposit MoN-Ag films: Ag reflexes occur at several positions in the X-ray pattern with crystallographic orientations of (111), (200), (220), (311) and (222). Additionally, peaks of γ-Mo_2N can be observed. The Ag phases seem to be stress-free, but the γ-Mo_2N phase shows significantly shifted peaks to lower angles, maybe caused by compressive stress (see, e.g., (111), (002) and (022)).

In Figure 9b XRD patterns of samples of the series HiP-0.07 are presented. A HiPIMS process with reduced nitrogen partial pressure (0.07 Pa) was used to deposit these coatings. No Ag-free film debris sample was available for the XRD measurements. Only the γ-Mo_2N phase can be identified in the XRD patterns of all three investigated MoN-Ag films. Even for the highest Ag content in the coatings (26.1 at.%, target MoAg35) no Ag precipitations are visible. We assume silver forms small clusters and due to their small crystallite size the phase is cryptocrystalline and not visible in the XRD patterns. The XRD patterns of the MoN-Ag films of the MoAg10 and MoAg20 targets are nearly identical with a preferential (002) texture. The shift of the X-ray peaks to lower angles indicates residual stress in the debris of the two films. The texture composition changes for the MoN-Ag film deposited from the MoAg35 target. The intensity of the (111) crystallographic orientation is now slightly higher than the (002) peak. Furthermore, additional peaks of the γ-Mo_2N phase occur at 2θ angles of 63.2° and 75.8°. The peaks of the film deposited from the MoAg35 target are not shifted.

Samples from another HiPIMS series (HiP-0.4) manufactured at the same nitrogen partial pressure as the dcMS sputtered films are shown in Figure 9c. The Ag-free MoN film possesses only peaks of the δ-MoN phase. Incorporating Ag into the film changes the crystallographic structure completely. Mainly peaks of the γ-Mo_2N phase can be identified. Due to the possible peak shifting caused by stresses and possible preferred orientation in the MoN-Ag film debris, it cannot unequivocally be concluded that no δ-MoN phase is also present. However, the fraction of this phase will be negligible. Furthermore, no distinct Ag peak could be identified. Only the asymmetric shape of the (111) peak of γ-Mo_2N (MoAg35 target)) could be a hint on tiny Ag precipitations.

The identified crystallographic phases of all investigated MoN and MoN-Ag films are compiled in Table 3.

Table 3. Compilation of the crystallographic phases identified for the MoN and MoN-Ag films. In brackets are phases which have not unequivocally been identified.

Target	Crystallographic Phases		
	dc-0.4	HiP-0.07	HiP-0.4
Mo	Mo [1], δ-MoN	-	δ-MoN
MoAg10	γ-Mo_2N, δ-MoN	γ-Mo_2N	γ-Mo_2N, (δ-MoN)
MoAg20	γ-Mo_2N, δ-MoN, (Ag)	γ-Mo_2N	γ-Mo_2N, (δ-MoN)
MoAg35	γ-Mo_2N, Ag	γ-Mo_2N	γ-Mo_2N, (Ag)

[1] The Mo phase originates from the Mo adhesion layer used only in this sample.

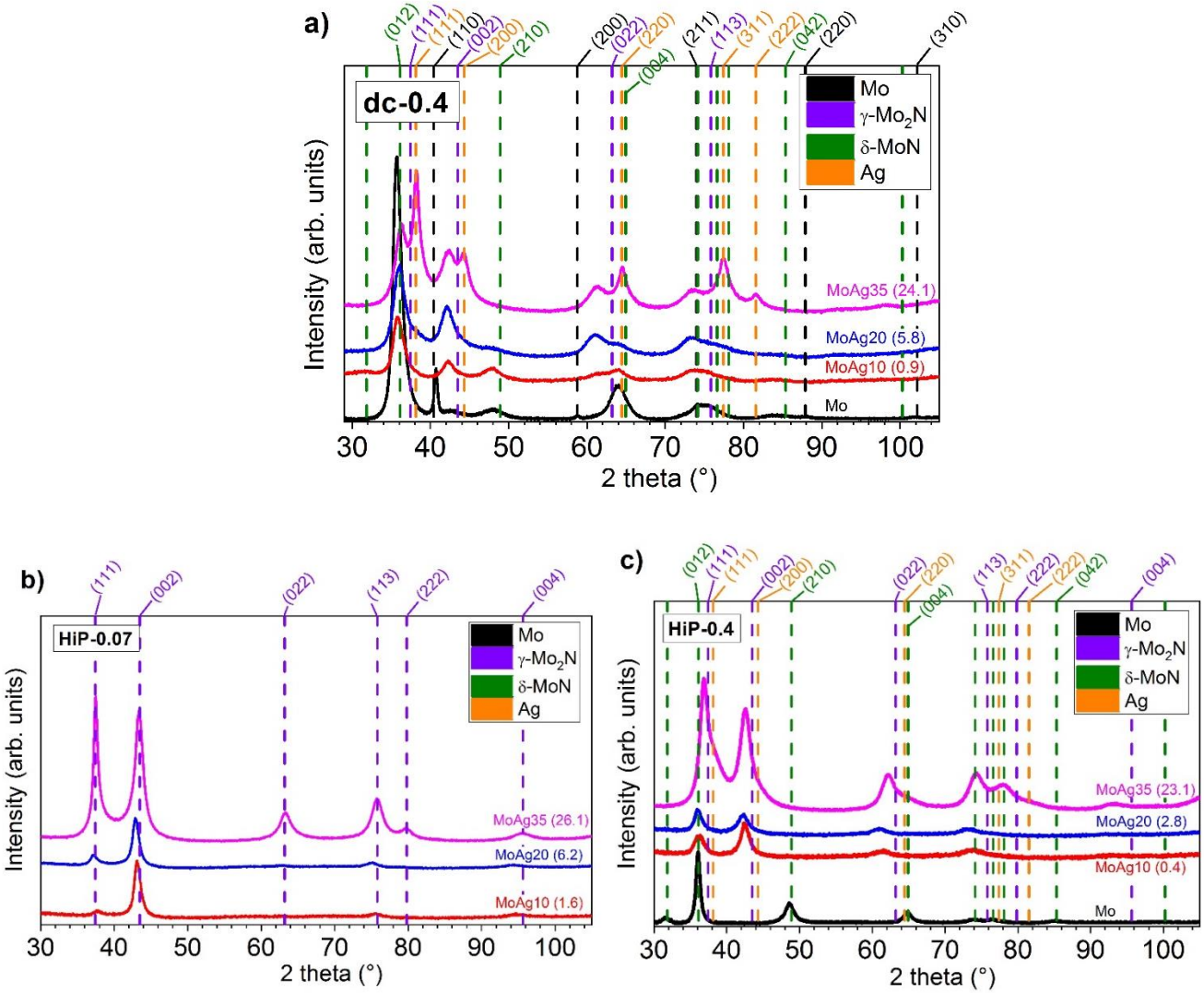

Figure 9. XRD patterns of Mo_xN and MoN-Ag films: (**a**) series dc-0.4, (**b**) series HiP-0.07 (the Ag-Figure 2. N film is missing) and (**c**) series HiP-0.4. The main X-ray peaks of Mo, γ-Mo_2N, δ-MoN and Ag have been included as vertical dashed lines. The Ag content of the coatings is added in brackets (in at.%) to the MoAg target materials.

3.4. Microhardness

Well adherent coatings with HF class of 1–3 have been deposited. Figure 10 shows the microhardness of the MoN-Ag coatings as a function of the Ag content. Silver-free MoN coatings have an indentation hardness H_{IT} of 23.1 (dc-0.4), 25.0 (HiP-0.07) and 31.2 GPa (HiP-0.4). Both HiPIMS-MoN films show a higher hardness compared to the dcMS film, whereas the hardest MoN film has a similar N content as the dcMS film, but an 8 GPa

higher hardness. However, adding 0.4 at.% Ag into this hardest MoN films leads to a significant drop in hardness to 22.1 GPa. This certainly is caused by the loss of the pure δ-MoN structure, as shown in the previous section, as this phase is harder compared to γ-Mo_2N [28]. With increasing Ag content all three MoN-Ag film series show a more or less pronounced decrease in hardness. The dcMS-0.4 and the HiP-0.4 MoN-Ag film series show a very similar progression of the hardness values with respect to the Ag content. The HiP-0.7 MoN-Ag films possess higher hardness. For these sample series, a hardness decrease occurs only at Ag contents higher than 6 at.%. The pronounced hardness increase with the Ag content, as reported by Gulbiński et al. [15], was not observed for our MoN-Ag film series. They used pulsed magnetron sputtering and a low substrate bias voltage for film deposition. The hardness increase was ascribed to a dispersion of silver atoms into the nitride lattice. This induces its distortion resulting in hardness enhancement. Furthermore, silver sub-nanometer clusters cause a re-nucleation of the nitride lattice leading to a crystallite size refinement [15]. According to the Hall–Petch relationship, the reduction in grain size increases the hardness of materials [29,30]. For silver-rich films, the presence of the soft component facilitates the grain boundary sliding, leading to the drop of hardness [15,19].

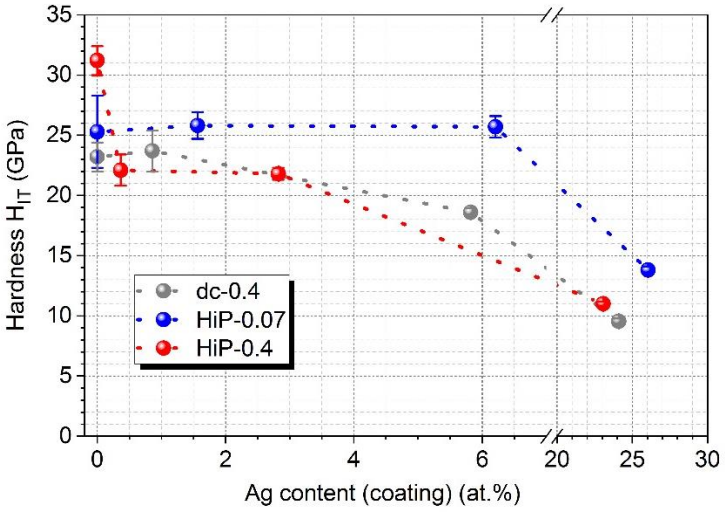

Figure 10. Indentation hardness H_{IT} vs. Ag content of the MoN-Ag coatings.

The influence of a substrate bias voltage on hardness and Ag content of MoN-Ag coatings is presented in Figure 11. The process HiP-0.4 (MoAg35 target) was used as a base for having the maximum i_{peak} and thus ionization of the sputtered atoms. Obviously, an increase of the bias voltage from floating to −150 V linearly increases the hardness from 11 GPa to 17.6 GPa. This is accompanied by a linear decrease of the Ag content in the MoN-Ag coatings. Hence, the removal of the soft Ag phase caused by bias-induced preferential sputtering leads to the hardness increase. The Ag content drops by a factor of about 2 from 23.1 at.% (floating) to 11.6 at.% (−150 V). Given the Ag concentration in the targets purchased, the substrate bias turned out to be the only method to produce coatings with Ag content between 6 and >20 at.% Ag. Therefore, this considerable influence on hardness and Ag content has to be taken into account when applying a bias voltage to the substrates. Otherwise, a very compact film structure is obtained already with a bias voltage of −30 V as can be observed in SEM micrographs of fracture cross sections shown in Figure 8. A slightly denser microstructure is even found for higher bias voltages.

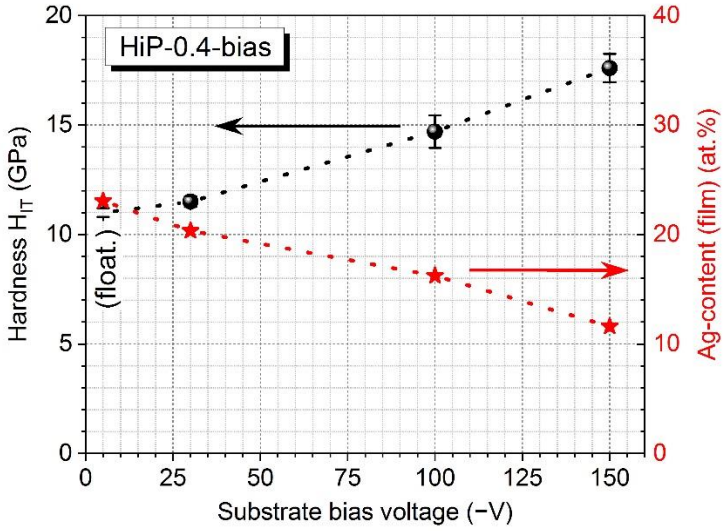

Figure 11. Indentation hardness H_{IT} and Ag content vs. substrate bias voltage of the MoN-Ag coatings deposited with a MoAg35 target.

The hardness values presented in this Section are quite comparable with the ones reported by Gulbiński et al. [15]. They observed a hardness of 20 GPa for a Ag content of about 6 at.%, which was identified as optimum Ag content for tribological behavior.

3.5. Tribological Properties

In Figure 12 the results of pin-on-disc tribotests at room temperature (RT) on MoN and MoN-Ag films are presented. Two typical friction curves (RT and HT) have already been shown in Figure 1, which illustrated that the COF is stable during long-term operation with a relatively smooth curve behavior. Figure 12a shows the average COF and Figure 12b the wear rate. For Ag-free MoN films, a low COF of 0.23–0.29 is measured. The low COF of most of the MoN and MoN-Ag films is explained by adsorbed water, which, together with surface oxide traces, builds a lubricating layer [15]. Incorporating Ag into MoN films leads to different tribological behavior with respect to the sputtering process:

1. dc-0.4: The Ag content seems to have no significant impact on the COF. For Ag contents of 1–24 at.% the COF is in the range of 0.23–0.26. The wear rate is linearly increasing with increasing Ag content.
2. HiP-0.07: The COF of MoN-Ag films is decreasing with increasing Ag content, reaching a minimum at about 6 at.% Ag and then increasing to a COF of 0.49 at a Ag content of 26 at.%, which is the highest COF of all studied samples (at RT). The wear rate of the samples from this series is lower than from the other two series, but at a Ag content of about 6 at.% the wear rate is only slightly lower than the one of the dc-0.4 series.
3. HiP-0.4: The COF vs. Ag content shows a quite similar behavior as HiP-0.07 sputtering process. However, the COF of the highest Ag content is significantly lower compared to the sample of the HiP-0.07 sputtering process, scoring a value of 0.37 at a Ag content of 23 at.%. The wear rate at a Ag content of 0.4 at.% is the same as for the one of the dc-0.4 series. However, it strongly deviates to higher wear rates for a Ag content of 2.8 at.%, i.e., with a wear rate of 0.36×10^{-6} mm^3/Nm it possesses the highest wear. This deviation is remarkable, as the COF for the MoN-Ag films is nearly identical at these Ag contents.

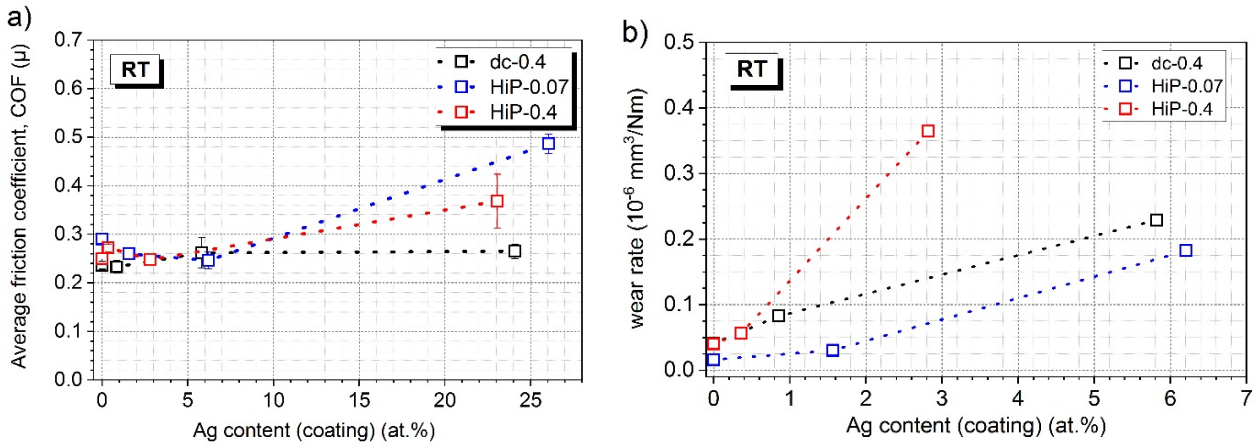

Figure 12. COF (**a**) and wear rate (**b**) of MoN-Ag coated steel vs. Ag content studied by pin-on-disc tests with Al_2O_3 counterpart at room temperature (30,000 rotations).

The COFs and wear rates of pin-on-disc tribotests at high temperature (HT, 450 °C) on MoN and MoN-Ag films are presented in Figure 13a,b, respectively. The COF of the MoN samples from the three sputtering processes is higher at HT as for the ones at RT (Figure 13a). The highest COF of 0.55 is measured here for the dc-0.4 sample compared to roughly 0.4 for both HiPIMS deposited ones. Besides this difference, the COF was found to decrease with increasing Ag in a very uniform manner for all three sputtering processes, i.e., at the same Ag content, all MoN-Ag coated samples practically have the same COF irrespective of the sputtering process. The lowest COF of about 0.25–0.27 is observed for samples possessing a Ag content in the range of 23–26 at.%.

Compared to the tribotests at RT, far higher wear rates are measured for the HT tribotests (Figure 13b). With an HT wear rate of 9×10^{-6} mm^3/Nm the MoN-coated steel sample from the dc-0.4 series again shows the worst tribological behavior compared to all other samples ($\leq 2 \times 10^{-6}$ mm^3/Nm). At small Ag contents (0.4–1.6 at.% Ag) the wear rates amount to around 2×10^{-6}, at medium Ag contents (2.8–6.2 at.% Ag) they decrease to around 1×10^{6} mm^3/Nm. Thus, it seems that the sputtering process (dcMS or HiPIMS) is less important for the tribological behavior of MoN-Ag coated steel samples than the Ag content. Hence, it is more important to precisely adjust the Ag content in the films—which is somewhat challenging for sputtering from MoAg compound targets—than to choose an advanced sputtering process. However, this fact may partly also be owed to the missing substrate bias voltage, which would densify the film's microstructure.

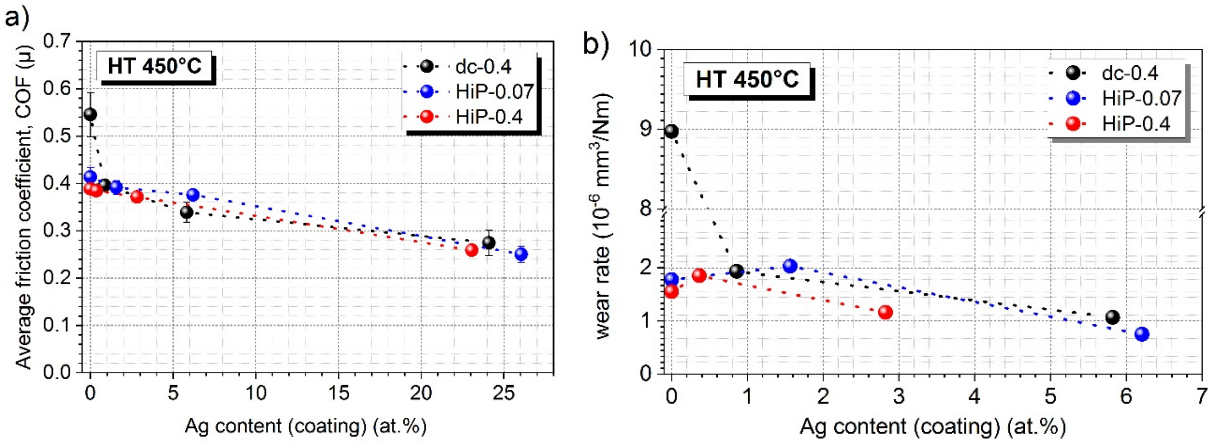

Figure 13. Friction coefficient (**a**) and wear rate (**b**) of MoN-Ag coated steel vs. Ag content of pin-on-disc tests at 450 °C (30,000 rotations). Notice: the y axis is interrupted between the numbers 3 and 8.

The results from tribological tests at RT and HT have been compiled in Figure 14a,b. This comparison is interesting for applications as for example for aerospace components [3], where a cycling from low temperatures (around RT) to elevated temperatures occurs. In the case of the COF (Figure 14a), the difference of the COFs due to the cycling between RT and HT varies between 0.1 and 0.14 except two samples (dc-0.4/Mo target and HiP-0.07/MoAg35 target). That means that, on average, the influence of the temperature in the investigated temperature range on the COF is negligible. Surprisingly, the difference of the COF of the sample dc-0.4/MoAg35 amounts to only 0.01. Different behavior can be observed for the comparison of the wear rate (Figure 14b). The wear rate of the coated samples from the HT tribotests is considerably higher with respect to the relevant samples from RT tribotests, i.e., the wear of the coated samples is governed by the behavior at HT during cycling. Hence, the increase in wear rate for the samples at RT with increasing Ag content (Figure 12b) does not play an important role. The reduction of the wear rate at HT with increasing Ag content is the most important factor for the tribological behavior of the coated samples during cycling. The lowest wear rates at HT after 30,000 rotations were observed for Ag contents of about 3–6 at.%. Gulbiński et al. [15] identified 6 at.% as optimum Ag content for tribological behavior. However, it cannot be excluded that a further enhancement of the tribological behavior may be found at somewhat higher Ag contents, which were not be covered by this research.

One sample strongly deviates from the other samples, with a relatively high wear rate: the sample dc-0.4/Mo target at HT. This is the sample with the highest COF. Here, a low amount of silver can significantly improve the tribological behavior.

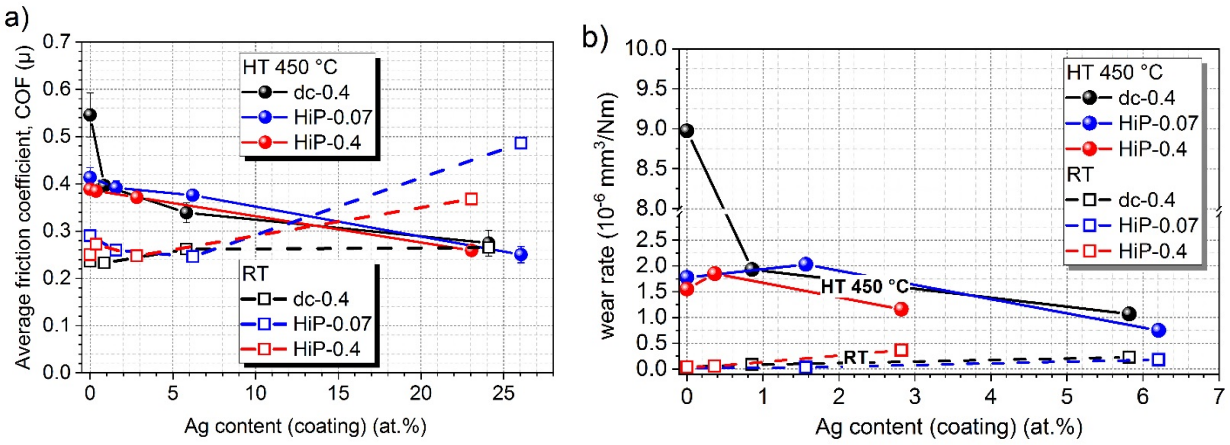

Figure 14. Comparison of the average friction coefficient (**a**) and wear rate (**b**) of MoN-Ag coated steel vs. Ag content studied by pin-on-disc tests with Al_2O_3 counterpart (30,000 rotations) at RT (dashed lines) and HT (compact line).

Pin-on-disk tribotests with 5000 rotations at both temperatures (RT, 450 °C) have also been rendered with the samples from the HiP-0.4-bias series (Figure 15). For both temperatures quite similar COFs have been recorded (Figure 15a). The highest deviation ($\Delta COF \approx 0.15$) is observed for the samples with the highest Ag content (sample at floating potential) with the higher COF found at RT. The wear rate (Figure 15b) almost linearly decreases with an increasing bias voltage (i.e., decreasing Ag content). However, the RT curve possesses a steeper slope. Therefore, the lowest wear rates are observed for the high bias voltages −100 and −150 V. We conclude, that applying a substantial substrate bias voltage is beneficial for the tribological behavior, despite the fact that a substantial amount of Ag is lost in the MoN-Ag films due to preferential sputtering. This can be regarded as an indication that the best tribological behavior at HT may be found in the Ag-content range between 6 and 15 at.% with an applied bias. However, a direct comparison with the other wear resistance test results is not possible due to the difference in the test duration.

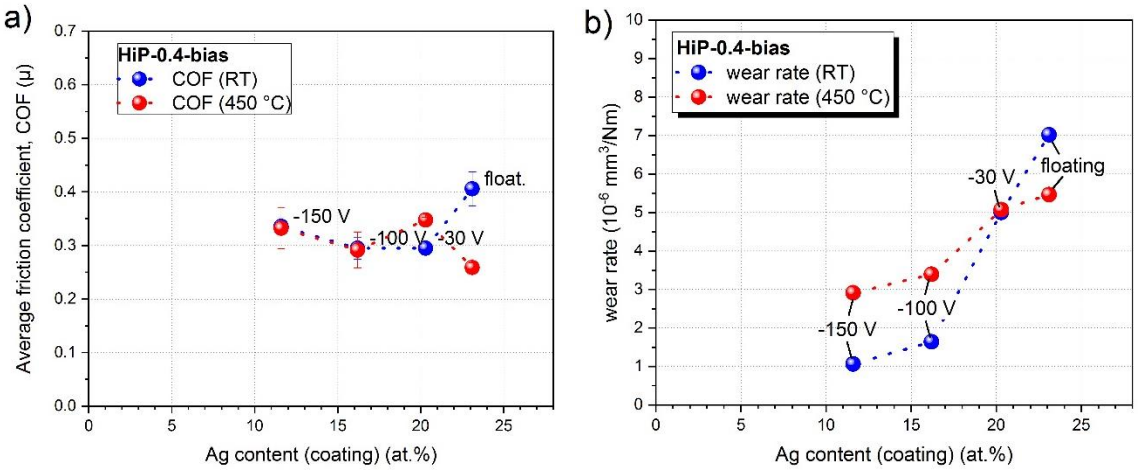

Figure 15. COFs (**a**) and wear rates (**b**) vs. Ag content of the samples from the bias series (HiP-0.4-bias) of pin-on-disc tests at RT and HT (450 °C, 5000 rotations).

Due to the high temperature (450 °C) during HT tribotests the film surface outside the wear track is also oxidized. Solak et al. [31] reported that the resistance of Mo_xN coatings to oxidation is poor because of their non-protective nature and the volatility of the oxides at moderately high temperatures. Mo_2N starts to oxidize at temperatures between 350 and 400 °C [31]. As outlined in Section 2.2, the oxide thickness of HT tribo-samples was measured after the tribotests by preparing a ball crater in a non-tested region of the sample and evaluating the ball crater-wear track by confocal microscopy. With this procedure, the dependence of oxide thickness on Ag content could be measured (Figure 16). The investigation shows that Ag-free MoN films contain the lowest oxide thickness of about 0.1–0.15 µm. Increasing the Ag content strongly increases the oxide thickness. At higher Ag content, the oxide thickness seems to saturate at values of 1.5–1.6 µm. The oxidation of the MoN-Ag films leads to film volume increase. The remaining (non-oxidized) MoN-Ag film is still in the range of 1.2–1.4 µm. Hence, these samples are oxidized to nearly half of their total coating thickness after oxidation. Two data sets from series HiP-0.07 in Figure 16 are labelled by blue ellipses (Ag content: 1.6 and 6.2 at.%). Due to the deviation from the fitted exponential lines, the measurements have been repeated. However, nearly identical oxide thicknesses have been measured for the same Ag contents. At present, it is not clear why the oxide thickness is distinctly lower for the MoN-Ag film with 6.2 at.% Ag compared to that with 1.6 at.% Ag despite the higher Ag content. Different coating properties influence the oxidation behavior:

- Crystalline phase structure: Mo_2N coating material showed a higher oxidation threshold compared to MoN [1]. However, according to Figure 9b both MoN-Ag films possess the same nitride phase: i.e., γ-Mo_2N (curves MoAg10 and MoAg20).
- Chemical composition: Figures 5 and 6 revealed that the MoN-Ag coating with 1.6 at.% of Ag (MoAg10 target) is N-deficient, whereas the one with 6.2 at.% (MoAg20 target) has 10 at.% less Mo in the film. Maybe N-deficient Mo2N is more easily oxidized (no reference has been found for this statement).
- Film microstructure: The MoN-Ag coating deposited with the MoAg10 target shows a columnar microstructure, whereas the coating deposited by MoAg20 lost its columnar structure (Figure 7). According to Musil et al. the oxidation of thin films can occur at the grain boundaries of thin films [32]. Hence, a columnar structure facilitates the oxidation process.

Therefore, the difference in oxide coating thickness of the two discussed MoN-Ag films might be traced back to the chemical composition and the microstructure.

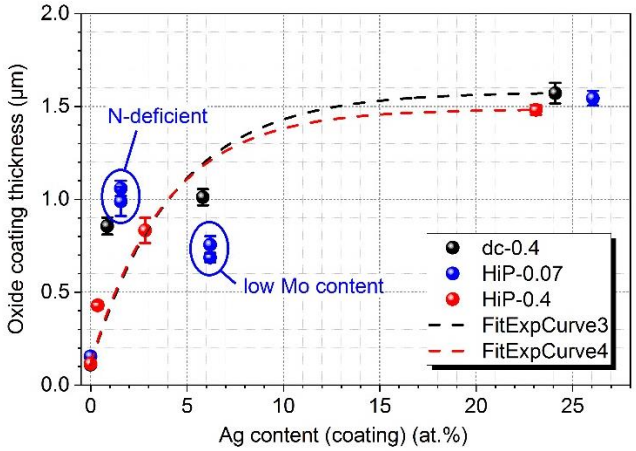

Figure 16. Oxide coating thickness vs. Ag content of MoN-Ag coated steel samples from tribological tests at 450 °C.

3.6. Raman Measurements

As described in Section 2.2 Characterization, two different Raman spectrometers have been used for Raman measurements on the samples of HT tribotests: (a) macro Raman measurements with a laser spot diameter of 1.1–1.6 mm and (b) micro Raman measurements with laser spot diameters of 5 and 30 µm.

Macro Raman measurements of the MoN-Ag films outside the wear track are compiled in Figure 17. The $Ag_2Mo_4O_{13}$ phase [15] was only observed for the MoN-Ag films deposited with the MoAg35 target in all three deposition series (Figure 17a–c). All other occurring peaks belong to the MoO_3 phase [12,15,33,34] and are listed in Table 4. The major difference between the three samples made with the MoAg35 target is found in the intensity of the 950 cm^{-1} line. The dc-0.4 shows the highest intensity, whereas the HiP-0.07 shows the lowest. This seems to correlate with the occurrence of Ag precipitations, as can be observed in the XRD patterns of Figure 9a,c and also in the SEM image of dc-0.4/MoAg35 in Figure 7. Maybe these Ag agglomerates in the as-deposited films promote the Ag diffusion to the surface and its reaction with the oxidizing MoN surface in contrast to the more evenly distributed Ag atoms of sample HiP-0.07/MoAg35. The other phases which occur in Figure 17b,c also belong to the MoO_3 phase. As written in Section 3.5 oxidation of MoN to MoO_3 already starts between 350 and 400 °C [31]. The Raman spectra of Figure 17 are quite similar to the ones reported by Gulbinski et al. [15] for HT tribotests at 400 °C.

Table 4. Measured peaks of MoO_3 phase in the Raman spectra of Figures 17 and 18. The intensities are given in brackets as w = weak, m = medium, s = strong and vs = very strong.

Frequencies (cm^{-1}) and Intensities of Raman Spectra of MoO_3 Phase							
82.9 (w)	97.7 (w)	115.5 (m)	127.3 (m)	155.3 (s)	197.7 (w)	216.7 (w)	244.3 (w)
283.4 (s)	336.6 (m)	365.1 (w)	377.9 (w)	469.9 (w)	666.6 (m)	819.2 (vs)	994.7 (vs)

The spectra of the micro Raman measurements of the bias series (HiP-0.4-bias) acquired outside the wear track of the samples after HT tribotests are shown in Figure 18. The substrate bias voltage seems to have a significant influence on the formation of the $Ag_2Mo_4O_{13}$ phase. This phase can still be observed but is strongly reduced. As discussed in Section 3.2 (Figure 8), this can be traced back to the change in the microstructure, which was already identified for a bias voltage of −30 V. Presumably, more compact film microstructure hinders the Ag diffusion towards the coating surface, necessary for its reaction with the oxidizing MoN coating to synthesize the $Ag_2Mo_4O_{13}$ phase.

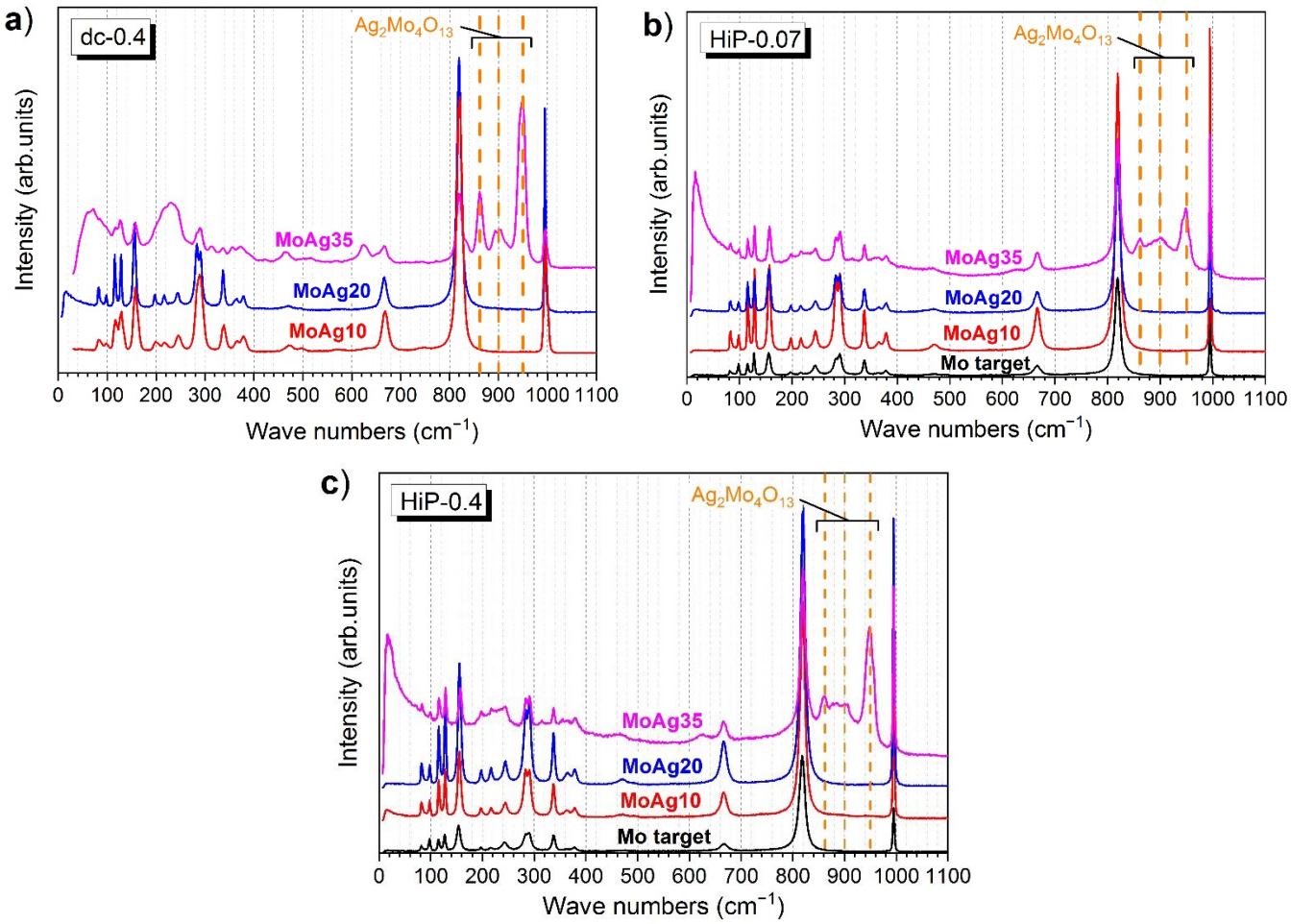

Figure 17. Macro Raman measurements. Spectra taken outside the wear track of samples after HT tribotests. The spectra in (**a**) are from series dc-0.4, in (**b**) from HiP-0.07 and in (**c**) from HiP-0.4.

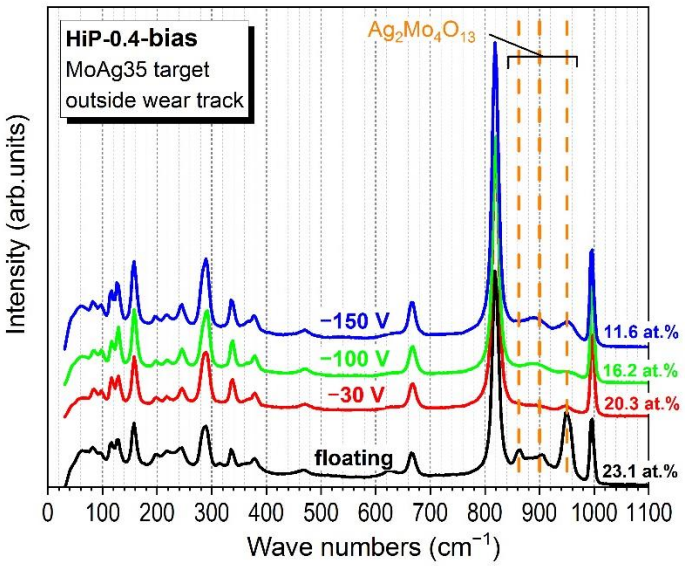

Figure 18. Micro Raman measurements. Spectra of the bias series (HiP-0.4-bias) taken outside the wear track of samples after HT tribotests with a laser spot size of 30 µm. The curves are labelled with the applied substrate bias and the Ag content on the right side.

In order to gain information about Ag molybdates from inside and beside the wear tracks, micro Raman measurements with a spot size of 5 µm have been performed across the wear track on the samples after HT tribotests and are shown in Figure 19.

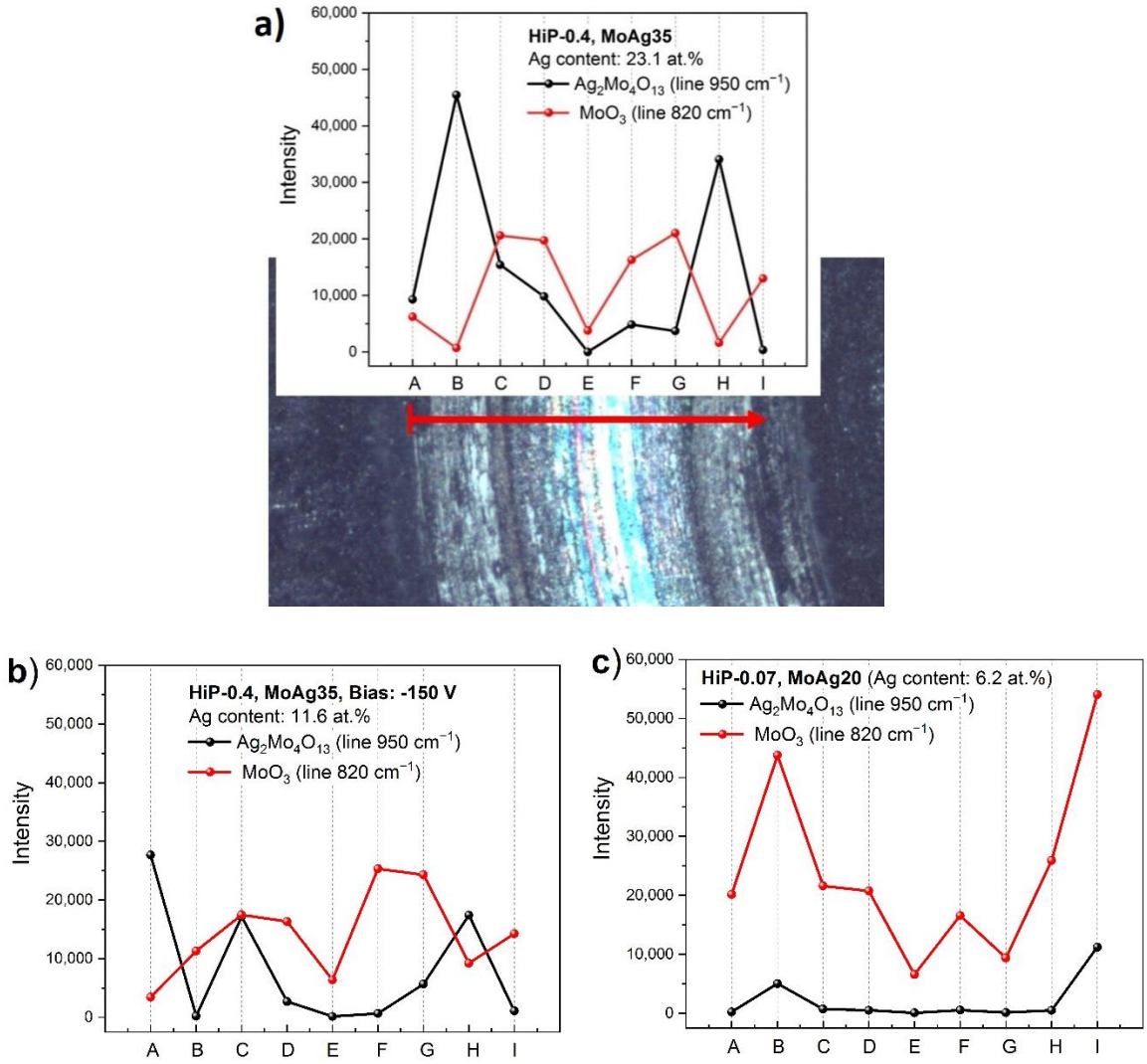

Figure 19. Micro Raman measurements across the wear track after HT tribotests for MoN-Ag coated steel samples with (**a**) 23.1 at.% Ag (HiP-0.4, MoAg35), (**b**) 11.6 at.% Ag (HiP-0.4-bias, MoAg35) and (**c**) 6.2 at.% Ag (HiP-0.07, MoAg20). The length of the red arrow in Figure 19a is about 400 µm (corresponds to wear track width). The Raman intensity of the 820 cm^{-1} line for MoO_3 (red line) and the Raman intensity of the 950 cm^{-1} line (black line) for $Ag_2Mo_4O_{13}$ are plotted vs. the length across the wear track. The measurement positions (A, B, . . . , I) across the wear tracks are estimated.

In Figure 19a a photograph of the wear track including the path of the Raman measurements (=red arrow) and a diagram is shown. In the diagram, the Raman intensity vs. the path length is plotted, and it is arranged in a way that the measurement length matches with the location of the red arrow. In Figure 19b,c the same diagrams are presented but without the photographs of the wear tracks. The Raman measurements in Figure 19 are only for qualitative evaluation to visualize the courses of the MoO_3 and $Ag_2Mo_4O_{13}$ phases across the wear tracks. In Figure 19a,b it was found that the $Ag_2Mo_4O_{13}$ phase is preferably located at the rim of the wear track. More precisely, the highest $Ag_2Mo_4O_{13}$ intensities were found by intentionally measuring on whitish wear debris at the rim of the wear tracks. Far lower intensities were partially also measured on Ag clusters located between the center and the rim of the wear track. The MoO_3 phase is highest within the wear track. The diagram of the sample with the lower Ag content of 6.2 at.% (Figure 19c)

looks quite different. The Ag content is too low for the formation of high amounts of $Ag_2Mo_4O_{13}$ phase. However, this phase is also found with lower intensities and again, it is only located at the rim of the wear track in the wear debris. For this sample, the highest amounts of MoO_3 phase are measured and these are now also found in the wear debris. Likewise, Gulbiński et al. [15] reported that for samples containing 6 at.% Ag, the first traces of phases (molybdate phases) other than MoO_3 have been found in Raman spectra taken from the wear track area after 400 °C tests. Their conclusion was that the molybdate synthesis is tribo-activated.

The Raman measurements revealed that at low Ag contents (≈6 at.% and below) and at temperatures of 450 °C only negligible amounts of the $Ag_2Mo_4O_{13}$ phase can be synthesized within the wear track (Figure 19c). Since the oxidation of the Mo_xN is strongly increased by even low amounts of Ag (Figure 16), the friction reduction at these low Ag contents may more probably be governed through the MoO_3 phase. At higher Ag contents (≈20 at.%) the $Ag_2Mo_4O_{13}$ phase was also identified outside the wear track, i.e., the environmental temperature is sufficient to form this Ag molybdate phase. For lower Ag contents (about 6–20 at.%) the frictional heating with its occurring flash temperatures [35] is necessary for the tribochemical synthesis of Ag molybdates.

4. Conclusions

MoN and MoN-Ag coatings have been deposited by dcMS and HiPIMS from MoAg composite targets onto HSS substrates. The addition of silver to MoN has a significant influence on the coating's microstructure, hardness, oxidation behavior and tribological behavior. With Ag addition, a shift of the crystalline phase δ-MoN towards γ-Mo_2N was observed, the oxidation resistance in air was decreasing, and the COF and wear rate were improving for low Ag contents at HT. However, wear rates could only be acquired up to about 6 at.% Ag content, due to completely worn coatings for higher Ag contents. For up to 6 at.% Ag content in the coatings it was observed, that the wear rates of the coated samples from the HT tribotests are considerably higher with respect to the relevant samples from RT tribotests. Furthermore, the COF is roughly 0.1 higher for the HT case. The reduction of the wear rate at HT with increasing Ag content is the critical factor for the tribological behavior of the coated samples during cycling, as the wear rate at HT is much higher compared to the one at RT. The lowest wear rates at HT were observed for Ag contents of about 3–6 at.%. At HT, solid lubricants have been identified: MoO_3 at low Ag contents (<6 at.%) and Ag, MoO_3 and $Ag_2Mo_4O_{13}$ phase beyond. Hard coatings (>18 GPa) could be synthesized at Ag contents below about 11 at.%, depending on the deposition process and the substrate bias voltage. Further studies on MoN-Ag coatings are intended, especially with Ag contents in the range of 6–20 at.%. This was not possible with the used composite targets (and low bias voltages). Furthermore, tribological tests in the temperature range between RT and 450 °C should be performed.

Author Contributions: Conceptualization, M.F., M.B. and F.S.; Formal analysis, M.B.; Investigation, M.B., S.K., A.R. and T.V.; Methodology, M.F., M.B. and F.S.; Supervision, M.F., F.S. and T.P.; Writing—original draft, M.F.; Writing—review and editing, M.B., S.K., T.P., A.R. and T.V. All authors have read and agreed to the published version of the manuscript.

Funding: This research was funded by the German Research Foundation (DFG), grant number FE 613/9–1. TP and TV acknowledge support from European Regional Development Fund (project CZ.02.1.01/0.0/0.0/16–019/0000778).

Institutional Review Board Statement: Not applicable.

Informed Consent Statement: Not applicable.

Data Availability Statement: Data sharing is not applicable to this article.

Acknowledgments: The authors would like to thank the staff at fem: B. Schöne and R. Bretzler for SEM and WDX measurements, P. Neher for pin-on-disk tests at RT and H. Merz for GDOES studies.

Conflicts of Interest: The authors declare no conflict of interest.

References

1. Gassner, G.; Mayrhofer, P.H.; Kutschej, K.; Mitterer, C.; Kathrein, M. Magnéli phase formation of PVD Mo–N and W–N coatings. *Surf. Coat. Technol.* **2006**, *201*, 3335–3341. [CrossRef]
2. Ürgen, M.; Eryilmaz, O.L.; Çakir, A.F.; Kayali, E.S.; Nilüfer, B.; Işik, Y. Characterization of molybdenum nitride coatings produced by arc-PVD technique. *Surf. Coat. Technol.* **1997**, *94*, 501–506. [CrossRef]
3. Aouadi, S.M.; Paudel, Y.; Luster, B.; Stadler, S.; Kohli, P.; Muratore, C.; Hager, C.; Voevodin, A.A. Adaptive $Mo_2N/MoS_2/Ag$ Tribological Nanocomposite Coatings for Aerospace Applications. *Tribol. Lett.* **2008**, *29*, 95–103. [CrossRef]
4. Magnéli, A. Structures of the ReO_3-type with recurrent dislocations of atoms: 'homologous series' of molybdenum and tungsten oxides. *Acta Cryst.* **1953**, *6*, 495–500. [CrossRef]
5. Jehn, H.; Ettmayer, P. The molybdenum-nitrogen phase diagram. *J. Less Common Met.* **1978**, *58*, 85–98. [CrossRef]
6. Gilewicz, A.; Warcholinski, B.; Murzynski, D. The properties of molybdenum nitride coatings obtained by cathodic arc evaporation. *Surf. Coat. Technol.* **2013**, *236*, 149–158. [CrossRef]
7. Jehn, H.A.; Kim, J.-H.; Hofmann, S. Composition and properties of transition metal nitride thin films (ZrN, NbN, MoN). *Surf. Coat. Technol.* **1988**, *36*, 715–727. [CrossRef]
8. Shen, Y.G. Effect of deposition conditions on mechanical stresses and microstructure of sputter-deposited molybdenum and reactively sputter-deposited molybdenum nitride films. *Mater. Sci. Eng. A* **2003**, *359*, 158–167. [CrossRef]
9. Hones, P.; Martin, N.; Regula, M.; Lévy, F. Structural and mechanical properties of chromium nitride, molybdenum nitride, and tungsten nitride thin films. *J. Phys. D Appl. Phys.* **2003**, *36*, 1023–1029. [CrossRef]
10. Suszko, T.; Gulbiński, W.; Jagielski, J. The role of surface oxidation in friction processes on molybdenum nitride thin films. *Surf. Coat. Technol.* **2005**, *194*, 319–324. [CrossRef]
11. Zhu, X.; Yue, D.; Shang, C.; Fan, M.; Hou, B. Phase composition and tribological performance of molybdenum nitride coatings synthesized by IBAD. *Surf. Coat. Technol.* **2013**, *228*, S184–S189. [CrossRef]
12. Gulbiński, W.; Suszko, T.; Sienicki, W.; Warcholiński, B. Tribological properties of silver- and copper-doped transition metal oxide coatings. *Wear* **2003**, *254*, 129–135. [CrossRef]
13. Tung, S.C.; Cheng, Y.-T. Microstructures and tribological characteristics of electron-beam co-deposited Ag/Mo thin film coatings. *Wear* **1993**, *162*, 763–772. [CrossRef]
14. Zhang, W.; Zhang, X.; Xue, Q.; Yang, D. Microstructure and tribological characteristics of multilayer films deposited by ion-beam mixing. *Wear* **1996**, *197*, 266–270. [CrossRef]
15. Gulbiński, W.; Suszko, T. Thin films of Mo_2N/Ag nanocomposite—the structure, mechanical and tribological properties. *Surf. Coat. Technol.* **2006**, *201*, 1469–1476. [CrossRef]
16. Aouadi, S.M.; Paudel, Y.; Simonson, W.J.; Ge, Q.; Kohli, P.; Muratore, C.; Voevodin, A.A. Tribological investigation of adaptive $Mo_2N/MoS_2/Ag$ coatings with high sulfur content. *Surf. Coat. Technol.* **2009**, *203*, 1304–1309. [CrossRef]
17. Dai, X.; Wen, M.; Huang, K.; Wang, X.; Yang, L.; Wang, J.; Zhang, K. Toward low friction in water for Mo_2N/Ag coatings by tailoring the wettability. *Appl. Surf. Sci.* **2018**, *447*, 886–893. [CrossRef]
18. Murthy, A.P.; Govindarajan, D.; Theerthagiri, J.; Madhavan, J.; Parasuraman, K. Metal-doped molybdenum nitride films for enhanced hydrogen evolution in near-neutral strongly buffered aerobic media. *Electrochim. Acta* **2018**, *283*, 1525–1533. [CrossRef]
19. Turutoğlu, T.; Ürgen, M.; Çakır, A.F.; Öztürk, A. Characterization of Mo_2N/Ag Nanocomposite Coatings Produced by Magnetron Sputtering. *Key Eng. Mater.* **2004**, *264*, 489–492. [CrossRef]
20. Neumann, S.; Wüstefeld, C.; Motylenko, M.; Haus, L.; Bräunig, S.; Müller, M.; Rafaja, D. Microstructure and thermal stability of Mo-(Ag)-N coatings with high nitrogen content. *Surf. Coat. Technol.* **2018**, *352*, 257–264. [CrossRef]
21. VDI-Verlag. *VDI 3198 Beschichten von Werkzeugen der Kaltmassivumformung*; CVD- und PVD-Verfahren; VDI-Verlag: Duesseldorf, Germany, 1992.
22. Broitman, E.; Hultman, L. Adhesion improvement of carbon-based coatings through a high ionization deposition technique. *J. Phys. Conf. Ser.* **2012**, *370*, 012009. [CrossRef]
23. Anders, A.; Andersson, J.; Ehiasarian, A. High power impulse magnetron sputtering: Current-voltage-time characteristics indicate the onset of sustained self-sputtering. *J. Appl. Phys.* **2007**, *102*, 113303. [CrossRef]
24. Anders, A. Deposition rates of high power impulse magnetron sputtering: Physics and economics. *J. Vac. Sci. Technol. A Vac. Surf. Film.* **2010**, *28*, 783–790. [CrossRef]
25. Haye, E.; Colaux, J.L.; Moskovkin, P.; Pireaux, J.-J.; Lucas, S. Wide range investigation of duty cycle and frequency effects on bipolar magnetron sputtering of chromium nitride. *Surf. Coat. Technol.* **2018**, *350*, 84–94. [CrossRef]
26. Messier, R.; Giri, A.P.; Roy, R.A. Revised structure zone model for thin film physical structure. *J. Vac. Sci. Technol. A Vac. Surf. Film.* **1984**, *2*, 500–503. [CrossRef]
27. Mukherjee, S.; Gall, D. Structure zone model for extreme shadowing conditions. *Thin Solid Film.* **2013**, *527*, 158–163. [CrossRef]
28. Kommer, M. Korrelation zwischen Plasma- und Schichteigenschaften Beim System Mo-N bei dcMS-bzw. HiPIMS-Plasmaabscheidungen. Ph.D. Thesis, Friedrich-Schiller-Universität Jena, Jena, Germany, 2018.
29. Hall, E.O. The Deformation and Ageing of Mild Steel: III Discussion of Results. *Proc. Phys. Soc. B* **1951**, *64*, 747–753. [CrossRef]
30. Petch, N.J. The Cleavage Strength of Polycrystals. *J. Iron Steel Inst.* **1953**, *174*, 25–28.

31. Solak, N.; Ustel, F.; Ürgen, M.; Aydin, S.; Cakir, A.F. Oxidation behavior of molybdenum nitride coatings. *Surf. Coat. Technol.* **2003**, *174*, 713–719. [CrossRef]
32. Musil, J. Hard nanocomposite coatings: Thermal stability, oxidation resistance and toughness. *Surf. Coat. Technol.* **2012**, *207*, 50–65. [CrossRef]
33. Gulbiński, W.; Suszko, T. Thin films of MoO_3–Ag_2O binary oxides—The high temperature lubricants. *Wear* **2006**, *261*, 867–873. [CrossRef]
34. Haro-Poniatowski, E.; Jouanne, M.; Morhange, J.F.; Julien, C.; Diamant, R.; Fernández-Guasti, M.; Fuentes, G.A.; Alonso, J.C. Micro-Raman characterization of WO_3 and MoO_3 thin films obtained by pulsed laser irradiation. *Appl. Surf. Sci.* **1998**, *127*, 674–678. [CrossRef]
35. Holmberg, K.; Matthews, A. *Coatings Tribology: Properties, Mechanisms, Techniques and Applications in Surface Engineering*, 2nd ed.; Tribology and interface engineering series; Elsevier Science: Amsterdam, The Netherlands; Boston, MA, USA, 2009; ISBN 978-0-444-52750-9.